Environmental Science & Technology

pubs.acs.org/est

Article

Expiratory Aerosol pH: The Overlooked Driver of Airborne Virus Inactivation

Beiping Luo, Aline Schaub, Irina Glas, Liviana K. Klein, Shannon C. David, Nir Bluvshtein, Kalliopi Violaki, Ghislain Motos, Marie O. Pohl, Walter Hugentobler, Athanasios Nenes, Ulrich K. Krieger, Silke Stertz, Thomas Peter,* and Tamar Kohn*

Cite This: *Environ. Sci. Technol.* 2023, 57, 486−497

Read Online

ACCESS | Metrics & More | Article Recommendations | Supporting Information

ABSTRACT: Respiratory viruses, including influenza virus and SARS-CoV-2, are transmitted by the airborne route. Air filtration and ventilation mechanically reduce the concentration of airborne viruses and are necessary tools for disease mitigation. However, they ignore the potential impact of the chemical environment surrounding aerosolized viruses, which determines the aerosol pH. Atmospheric aerosol gravitates toward acidic pH, and enveloped viruses are prone to inactivation at strong acidity levels. Yet, the acidity of expiratory aerosol particles and its effect on airborne virus persistence have not been examined. Here, we combine pH-dependent inactivation rates of influenza A virus (IAV) and SARS-CoV-2 with microphysical properties of respiratory fluids using a biophysical aerosol model. We find that particles exhaled into indoor air (with relative humidity ≥ 50%) become mildly acidic (pH ∼ 4), rapidly inactivating IAV within minutes, whereas SARS-CoV-2 requires days. If indoor air is enriched with nonhazardous levels of nitric acid, aerosol pH drops by up to 2 units, decreasing 99%-inactivation times for both viruses in small aerosol particles to below 30 s. Conversely, unintentional removal of volatile acids from indoor air may elevate pH and prolong airborne virus persistence. The overlooked role of aerosol acidity has profound implications for virus transmission and mitigation strategies.

KEYWORDS: *influenza virus, SARS-CoV-2, aerosol acidity, airborne transmission, risk mitigation*

INTRODUCTION

Respiratory viral infections pose a great burden on human health. An average of 400,000 deaths are associated with influenza globally each year,[1] and the ongoing COVID-19 pandemic has already resulted in several million deaths and countless cases of long COVID around the world. To curb the public health and economic impacts of these diseases, health care policy aims to minimize virus transmission. Increasing evidence points to expiratory aerosol particles (see ref 2 for clarification of terminology) as vehicles for the transmission of influenza virus and SARS-CoV-2.[3] The persistence of these viruses in aerosols is still subject to scientific debate, with prior studies reporting highly variable rates of viral inactivation depending on the study design and choice of matrix.[4−6] Regardless, it is undisputed that rapid inactivation would contribute to limiting their spread.

Prior studies have investigated the effect of ambient conditions on the inactivation rates of aerosolized respiratory viruses including influenza virus,[5,7−11] SARS-CoV-2,[12−14] and the common cold human coronavirus HCoV-229E.[15] Relative humidity (RH) and temperature were the primary variables modulated in these works, with low (∼20%), medium (40−60%), and high (65−90%) RH compared at a few select temperatures. Some of these studies identified a "U-shaped" curve of inactivation as a function of RH,[7,10] and it has been suggested that RH affects virus inactivation by controlling evaporation of water from the aerosol particle, thus governing the concentration of inactivation-catalyzing solutes.[16−18] Furthermore, the physical processes of efflorescence and deliquescence due to varying RH have been suggested to influence surviving viral fractions of respiratory viruses.[19,20] In addition, the role of matrix composition including its protective effects on virus inactivation has been investigated.[5,10,21] Beyond this, the mechanisms of virus inactivation in aerosol particles remain largely speculative.

Received: August 12, 2022
Revised: December 6, 2022
Accepted: December 7, 2022
Published: December 20, 2022

A potentially powerful, yet understudied driver of airborne virus inactivation is the aerosol pH. It is established now that atmospheric aerosol particles can be highly acidic[22] and that some enveloped viruses, including influenza virus, are sensitive to low pH.[23] Nevertheless, even though previously hypothesized to be a determinant of virus fate,[24] the pH of expiratory aerosol particles, and hence its contribution to the inactivation of airborne viruses, remains poorly understood. The aerosol pH depends on the composition of the aerosol particle and the surrounding air, and it is well characterized for particulate matter equilibrated with inorganic acids and bases.[25] Recently, Oswin et al.[26] suggested that aerosol particles lose CO_2 upon exhalation, and they argue that the resulting alkaline aerosol pH (∼10) may account for the moderate inactivation of SARS-CoV-2 observed in their experimental system. However, the impact of air composition beyond RH and CO_2 has been overlooked to date. To the best of our knowledge, the only attempt to inactivate airborne viruses by modulating aerosol pH is the use of acetic acid from boiling vinegar during the 2002/03 outbreak of SARS-CoV-1 (see ref 27 and the Supporting Information).

Outdoor airborne particulate matter is often highly acidic, with pH values ranging between −1 and +5.[22,25] Contrary to expectations, the strength of the acid or base contained in aerosols (expressed by its dissociation constants) may not be the dominant parameter controlling aerosol pH. Rather, the volatility of species is of importance. For example, strong organic acids such as HCOOH and CH_3COOH partition negligibly to aerosol and bear a minor impact on aerosol pH for most atmospherically relevant conditions.[28] In contrast, HNO_3 and NH_3 partition into aerosol particles and impact pH, albeit buffered by the formation of ammonium nitrate.

Indoor aerosol particles have a variety of sources, including ventilation with outdoor air and human emissions from the respiratory tract, skin, and clothing. Indoor air tends to have lower levels of gas-phase inorganic acids (e.g., HNO_3) than outdoor air owing to their efficient removal via deposition on surfaces, as well as their condensation on indoor aerosol particles. Human activities are a source of organic acids and NH_3,[25,29,30] often elevating their levels compared to outdoors. The ratio of indoor to outdoor concentrations is typically 0.1−0.5 for HNO_3 and 3−30 for NH_3,[30] causing the pH of indoor aerosol particles to increase compared to outdoor levels. Operation of humidification, ventilation, and air conditioning systems also affects air composition[31] and, hence, likely the pH of indoor aerosol particles. While many outdoor and indoor aerosol particles are in equilibrium with their environment, this can only be expected for exhaled aerosol if given enough time. In the interim, freshly exhaled aerosol can change its pH considerably.

Exhaled air, before mixing into the indoor air, contains high concentrations of NH_3 and is characterized by very high concentrations of CO_2 and high number densities of expiratory aerosol particles. These particles are emitted by breathing, talking, coughing, or sneezing and contain a complex aqueous mixture of ions, proteins, and surfactants. Although the pH of exhaled breath condensate has been investigated, such measurements are often performed after deaeration by bubbling a noble gas through the sample, which leads to the loss of CO_2 and an increase of pH.[32] There is no study that quantifies the pH of respiratory aerosol when it equilibrates with the acidic or alkaline gases present in the indoor air within a few seconds to minutes of exhalation.

Here, we investigate the role of aerosol acidity in the inactivation of airborne influenza A virus (IAV) and two coronaviruses, SARS-CoV-2 and HCoV-229E, in indoor environments. We accomplish this in three steps by first determining the pH-dependent inactivation kinetics of IAV, SARS-CoV-2, and HCoV-229E in bulk samples of representative respiratory fluids, then measuring the thermodynamic and kinetic properties of microscopic particles of these fluids in an electrodynamic balance (EDB), and finally jointly applying the inactivation kinetics and aerosol properties in a biophysical model to determine inactivation in the aerosol system. We then use the model to investigate virus inactivation under a range of particle sizes and indoor air compositions. Finally, we assess the virus transmission risk under different interventions that modulate aerosol pH, including air filtration, NH_3 scrubbing, or enrichment with nonhazardous concentrations of HNO_3.

MATERIALS AND METHODS

Virus Inactivation Experiments. Experiments were conducted with three viruses [influenza virus strain A/WSN/33 (H1N1), SARS-CoV-2 strain BetaCoV/Germany/BavPat1/2020, and HCoV-229E-Ren] in three liquid matrices [synthetic lung fluid (SLF; see Table S1 for composition), mucus harvested from primary epithelial nasal cultures grown at the air−liquid interface (nasal mucus), or aqueous citric acid/Na_2HPO_4 buffer]. All details pertaining to virus propagation, purification, and enumeration, as well as to matrix preparation and composition, are given in the Supporting Information.

Virus inactivation curves were measured at room temperature in 2 mL glass vials (G085S-1-H; Infochroma), 500 μL PCR tubes (Sarstedt), or 1.5 mL plastic tubes (Eppendorf) using a matrix volume between 10 μL and 1 mL. Each experimental condition was tested in triplicate, except for a subset of SARS-CoV-2 experiments, which were performed in duplicate. IAV stock solutions were diluted with ultrapure distilled water (Thermo Fisher Scientific) to reach an approximate titer of 10^9 plaque forming units (PFUs)/mL. Virus stocks were then spiked into each test matrix to an initial experimental titer of 10^7 PFU/mL for IAV and HCoV-229E or 3×10^6 PFU/mL for SARS-CoV-2. After spiking, vials were vortexed at medium intensity for approximately 5 s, with the exception of SARS-CoV-2 samples, which were flick-mixed due to biosafety restrictions. The total exposure time was adjusted depending on the inactivation rate and ranged between 20 s for the lowest pH and 48 h for near-neutral pH. The sample pH stayed stable over the duration of the experiment. Samples were taken at regular time intervals (3 to 11 time points within each pH exposure) and were neutralized by diluting 1:100 in phosphate-buffered saline (PBS) for infection [PBSi; PBS containing 3% of bovine serum albumin solution 10% in DPBS (Sigma-Aldrich), 1% of P/S, and 1% of Ca^{2+}/Mg^{2+} 100 mM ($CaCl_2 \cdot 2H_2O$ and $MgCl_2 \cdot 6H_2O$, Acros Organics)]. The PBSi has a pH of 7.3. In most experiments with pH < 3.5, PBSi was supplemented with 2% of 10× citric acid−phosphate buffer at pH 7. Dilution in PBSi rather than addition of a strong base was chosen for sample neutralization because the latter approach was found to further decrease the virus titer. Neutralized samples were frozen until enumeration. To determine kinetic parameters, all replicate experiments of a given experimental condition were pooled. Inactivation rate constants were determined from least-square fits to the log-

https://doi.org/10.1021/acs.est.2c05777
Environ. Sci. Technol. 2023, 57, 486−497

linear portion of the inactivation curves, assuming pseudo-first order kinetics

$$\ln \frac{C}{C_0} = -k_{obs} \cdot t \quad (1)$$

Here, C is the virus titer at time t, C_0 is the initial virus titer, and k_{obs} is the observed inactivation rate constant. For measurements of C below the limit of detection (LoD), C was set to the LoD value. 99%-inactivation times (t_{99}) were determined based on k_{obs}

$$t_{99} = -\frac{\ln(0.01)}{k_{obs}} \quad (2)$$

Rate constants and associated 95% confidence intervals were determined using GraphPad Prism v.9.232. Control experiments were performed to confirm that virus titer loss at low pH could not be attributed to virus aggregation (Figure S1).

EDB Measurements of Aerosol Thermodynamics and Diffusion Kinetics. An EDB setup was used to measure the thermodynamic and kinetic properties of SLF and nasal mucus. The EDB measures the relative changes in mass and size of a single levitated particle as a result of changing RH; our specific setup is described in previous publications.[33,34] To generate the particles, we used concentrated SLF (1 mL of freeze-dried SLF in 400 μL of Millipore water) and freshly thawed nasal mucus. Briefly, a charged SLF/mucus droplet is injected with a droplet on demand generator (HP ink jet) into an environmental chamber (288.15 K) and levitated by an adjustable electric field.[35] The particle experiences two forces along the symmetry axis of the EDB: a gravitational force and a drag force induced by the gas flow through the chamber. Therefore, the DC voltage required to balance the particle in the center of the EDB is sensitive to the loss or uptake of water vapor. To induce gas-particle partitioning of water vapor at or near-equilibrium conditions, the RH in the chamber was slowly cycled between dry (<5%) and humid (ca. 90%) conditions by mixing dry and humidified N_2 flows. More rapid changes in RH allow inferring mass-transfer limitations by observing a delayed particle response.[36] The total flow was set to 20 sccm and controlled by mass flow controllers. The RH was measured with a capacitance sensor which is calibrated observing the deliquescence of various salts. Its accuracy was estimated to be ±1.5%. The particle size was determined by analyzing Mie resonances apparent in continuously recorded broad-band back scattering spectra.[34,37,38] The initial radius was estimated at 91% RH utilizing the resonance structure of Mie scattering.[39] An extended description of the EDB approach and data processing is given in the Supporting Information.

Biophysical Modeling. The Respiratory Aerosol Model ResAM is a biophysical model to determine virus inactivation times in the exhalation aerosol as a function of air composition. ResAM is based on a spherical shell diffusion model, which we have previously applied in physical and chemical contexts.[36,40,41] As novel input experimental data, ResAM uses the pH sensitivity of enveloped viruses and the thermodynamic and kinetic properties of respiratory fluids, both measured in the present work.

ResAM simulates the composition and pH changes inside an expiratory particle during exhalation. Hereby, we make the simplifying assumption that the mode of generation (breathing, coughing, and singing) does not influence the matrix composition. The model performs calculations for particles of selectable size (from 25 nm to 1 mm) with a liquid composed of H_2O, H^+, OH^-, Na^+, Cl^-, $CO_2(aq)$, HCO_3^-, $NH_3(aq)$, NH_4^+, $CH_3COOH(aq)$, CH_3COO^-, $CH_3COONH_4(aq)$, NO_3^-, as well as two classes of organic compounds with low and high molecular weight, representative of the lipids and proteins in the lung fluid (see subsection "Species treated by ResAM" in the Supporting Information for details).

The liquid phase is divided into concentric shells (Figure S2). The model treats 1−50 shells, depending on particle size (one shell for r = 0.02−0.1 μm and up to 50 shells for r = 1000 μm). The number of shells for each particle stays constant during the exhalation process. The shells are treated in a fully Lagrangian manner, that is, their thicknesses are calculated from the number of molecules of each species in a shell times their molecular volume, whereby diffusion processes between shells may cause each shell to evolve differently with time. By allowing the thickness of the shells to change, mass conservation is well satisfied (see the Supporting Information).

We take account of vapor pressures $p^{vap}_{H_2O}$, $p^{vap}_{NH_3}$, p^{vap}_{HCl}, $p^{vap}_{HNO_3}$, and $p^{vap}_{CH_3COOH}$ calculated using Henry's law coefficients listed in Table S2. The activity coefficients of H^+, Na^+, Cl^-, NO_3^-, and OH^- required for the vapor pressure and concentration simulation are calculated using the Pitzer ion-interaction model.[42,43] The activity coefficients of organic and neutral species are assumed to be unity, that is, they influence the physicochemical properties of SLF as ideal components simply via Raoult's law. SLF contains additional ions in minor concentration (Table S1). For all other minor anions, the activity coefficients of Cl^- and for the cations the activity coefficients of Na^+ are used. We obtain the liquid-phase diffusion coefficients of ionic and neutral species as well as the efflorescence RH values from our EDB measurements, assuming that the virus does not affect these properties [as preliminary experiments confirm (not shown)]. The liquid-phase diffusion coefficients D_l of the involved species in water are given in Table S3. In the absence of other information, we assume that D_l of all neutral species has the same dependence on water activity (a_w) as $D_{l,H_2O}(a_w)$ scaled with their value at infinite dilution. Similarly, the diffusivities of cations and anions are assumed to have the same dependence on a_w as Na^+ and Cl^-, respectively, again scaled with their dilute solution values from the literature. When RH decreases below efflorescence RH, we assume the resulting NaCl crystal to reside in the particle center and parameterize the effects of nonspherical symmetries, such as dendritic crystal growth, in terms of effective diffusivities (see more details on the related uncertainties in the Supporting Information).

We then use the model to calculate the pH value, and from this the corresponding virus inactivation rates, in each particle shell. The gas-phase compositions of exhaled air and the indoor air with purification and acidification are shown in Table S4. A detailed description of the ResAM model and its application to estimate virus inactivation and transmission risks is given in the Supporting Information. The current version of ResAM can readily be further refined beyond the conditions used herein, for example, to include a greater diversity of respiratory matrices or additional atmospheric gases.

RESULTS AND DISCUSSION

Kinetics of pH-Mediated Inactivation of Influenza Virus and Coronavirus. Inactivation kinetics of IAV, SARS-

https://doi.org/10.1021/acs.est.2c05777
Environ. Sci. Technol. 2023, 57, 486−497

CoV-2, and HCoV-229E were determined over a pH range from neutral to strongly acidic after immersion in bulk solutions of SLF, nasal mucus, or aqueous buffer. Figure 1

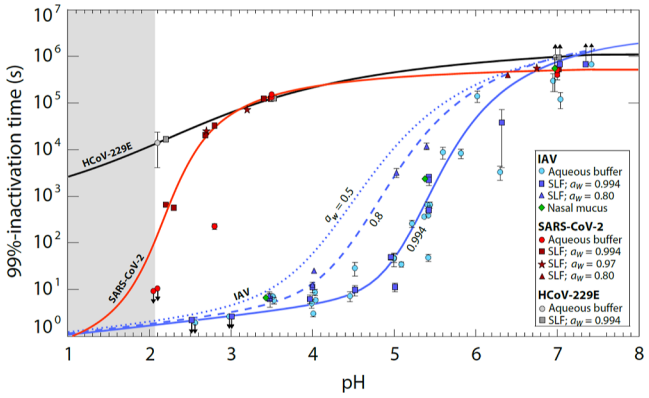

Figure 1. Time required for 99% titer reduction of IAV, SARS-CoV-2, and human coronavirus HCoV-229E in various bulk media. Data points represent inactivation times in aqueous citric acid/Na_2HPO_4 buffer, SLF, or nasal mucus with pH between 7.4 and 2, measured at 22 °C. SLF concentrations correspond to water activity a_w = 0.994 (1× SLF; squares), a_w = 0.97 (5× SLF; stars), and a_w = 0.8 (18× SLF; triangles); buffer (circles) and nasal mucus (diamonds) correspond to $a_w \approx 0.99$. Each experimental condition was tested in replicate with error bars indicating 95% confidence intervals. While IAV displays a pronounced reduction in infectivity around pH 5, SARS-CoV-2 develops a similar reduction only close to pH 2, and HCoV-229E is largely pH-insensitive. Solid lines are arctan fits to SLF data with a_w = 0.994 (blue: IAV; red: SARS-CoV-2; and black: HCoV-229E; see eqs S26−S28). The dashed line is an arctan fit to the SLF data with a_w = 0.80. The dotted line is a concentration-proportional extrapolation to a_w = 0.5 (24× SLF). Upward arrows indicate insignificant change in titer over the course of the experiment, and downward arrows indicate inactivation below the level of detection at all measured times. The fitted curves below pH 2 (gray shaded area) are extrapolated with high uncertainty. Examples of measured inactivation curves are shown in Figure S3.

summarizes the inactivation times (here expressed as the time to reach a 99% infectivity loss) as a function of pH. All viruses were stable in all matrices at neutral pH, with inactivation times of several days. From pH 6 to 4, IAV inactivation times decreased from days to seconds or by about 5 orders of magnitude. This decrease was evident in all matrices studied. It is noteworthy that inactivation in nasal mucus, which is most representative of the matrix comprising expiratory aerosol particles, is well described by SLF. However, inactivation times did depend on the SLF concentration. Specifically, we determined IAV inactivation at three different levels of SLF enrichment (1× and 18× SLF, determined experimentally; 24× SLF, determined by concentration-proportional extrapolation), corresponding to water activities a_w = 0.994, 0.8, and 0.5. This represents the fluid in equilibrium with a gas phase at 99.4, 80, and 50% RH, that is, from physiological equilibrium to common indoor conditions. The study of Lin et al.[44] suggests that the protective effect of proteins in the case of bacteriophages is concentration-proportional at high RH (80%) but is not as effective at lower RH (20−50%). Therefore, we assume that the concentration-proportional extrapolation is reasonable and might even become an overestimation at low RH. While inactivation times in aqueous buffer, 1× SLF, and nasal mucus were very similar, 18× enrichment of the SLF coincided with an increase in inactivation time by up to a factor of 56 (blue triangles in Figure 1). This protective effect of concentrated SLF was most prominent around the optimal pH for A/WSN/33 viral fusion of 5.1.[45] Coronaviruses were less affected by acidic pH than IAV. Both SARS-CoV-2 and HCoV-229E remained largely stable down to pH 3, where their inactivation still required 24 h. When further decreasing pH down to 2, the inactivation times rapidly reduced to <10 s for SARS-CoV-2 but never dropped below 2 h for HCoV-229E. Compared to aqueous buffer, SLF provided some protection against inactivation below pH 3, both at 1× and 5× SLF concentrations (while measurements for pH < 3 in 18× SLF were not possible due to precipitation). The measured differences in pH sensitivities between IAV and the coronaviruses may be explained by their different mechanisms of virus entry into host cells. IAV relies on an acid-induced conformational change in haemagglutinin during endosomal entry. This conformational change is

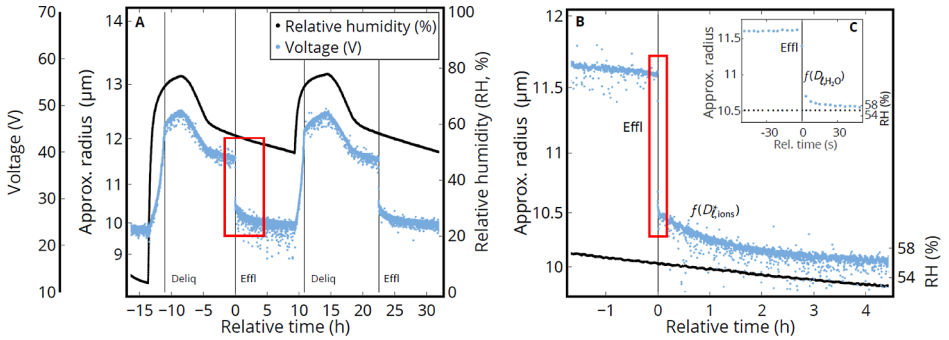

Figure 2. Measured hygroscopicity cycles of an SLF particle in an EDB forced by prescribed changes in RH. The voltage required to balance the particle in the EDB against gravitational settling and aerodynamic forces is a measure of the particle's mass-to-charge ratio, allowing the particle radius R to be estimated. (A) Two humidification cycles of an SLF particle with a dry radius $R_0 \approx 9.7$ μm. The experiment spanned about 2 days with slow humidity changes, allowing the thermodynamic and kinetic properties of SLF to be determined. Deliquescence/efflorescence points are marked by "Deliq/Effl". (B) Zoom on the drying phase [red box in (A)] with salts in the droplet (mainly NaCl) effloresing around 56% RH (black line): very fast initial crystal growth (<10 s) with rapid loss of H_2O from the particle, followed by slow further crystal growth (1 h). The latter is caused by the abrupt switch from H_2O diffusion to the diffusion of Na^+ and Cl^- ions through the viscous liquid, resulting in an ion diffusion coefficient of $D^*_{l,\mathrm{ions}} \approx 10^{-10}$ cm^2/s. The inset (C) highlights the minute before and after efflorescence, which allows a lower bound of the H_2O diffusivity to be determined, namely, $D_{l,\mathrm{H_2O}} > 10^{-7}$ cm^2/s.

https://doi.org/10.1021/acs.est.2c05777
Environ. Sci. Technol. 2023, 57, 486−497

irreversible;[46] if IAV encounters the fusion pH (typically pH < 5.5) outside the host cell, for example, while within an aerosol particle, the acid-triggered haemagglutinin can no longer bind to host-cell receptors and the virus is inactivated. Notably, IAV strains vary in their fusion pH optima[45] and therefore might also differ in their inactivation dynamics. Conversely, the spike glycoprotein of coronaviruses becomes fusion competent through cleavage by host proteases, instead of relying on acidic pH triggering conformational changes.[47] The different behavior of SARS-CoV-2 and HCoV-229E at pH < 3 remains unclear.

Thermodynamics and Diffusion Kinetics of Expiratory Particles. While Figure 1 shows the pH that must be attained in the aerosol particles for rapid virus inactivation, it lacks information on aerosol particle pH after exhalation into indoor air. To model the pH in these particles, it is essential to know the particle composition in thermodynamic equilibrium (liquid water content), as well as the kinetics that determine how rapidly the equilibrium is approached (water and ion diffusion coefficients). To obtain this information, we measured thermodynamic (equilibrium) and kinetic (diffusion-controlled) properties of individual micrometer-sized SLF and nasal mucus particles levitated contact-free in an EDB. Each particle was exposed to prescribed changes in RH (see Figure 2). Figure 2A shows two moistening/drying cycles of an SLF particle obtained over a period of 2 days. They allow determination of the particle equilibrium composition (water content or mass fraction of solutes, see Figure S4A) during time intervals with slowly changing RH. The particle clearly takes up and loses water when the RH is changed. It has a size growth factor at 90% RH of 1.3 (see also Figure S5) and deliquesces at 75%, indicating that NaCl is the predominant salt in the particle. Nasal mucus shows a similar size growth but deliquesces at 69% RH, indicating that it contains significant amounts of other hygroscopic compounds (Figure S5). We have no evidence for liquid−liquid phase separation in any of these particles (Figures S6A and S7), but Mie-resonance spectra indicate inhomogeneities in the particles even at high RH.

The kinetics of water uptake/loss as derived from periods with rapid RH change or efflorescence are highlighted in Figure 2. Figure 2B zooms in on one efflorescence event, first showing rapid water loss (<10 s) and then switching to a much slower rate of water loss over the next hour. This two-stage diffusion process was confirmed in measurements of additional SLF and nasal mucus particles (see Figure S8). We interpret this as fast initial dendritic growth of an NaCl crystal (Figure S6A−C), which depends on the ability of H_2O molecules to rapidly leave the particle and ends abruptly when the crystal reaches the droplet surface, followed by a slow crystal growth mode (Figure S6D), for which the diffusivity of the ions is crucial. In this representation, crystal growth is initially limited by the liquid-phase diffusivity of water molecules with $D_{l,H_2O} > 10^{-7}$ cm^2/s (Figure 2C), which are expelled from the particle as long as water activity is still high. Subsequently, the slow crystal growth is limited by the diffusivities of Na^+ and Cl^- ions through the progressively viscous liquid to the crystal (Figure S6D). From Figures 2B and S6D, we estimate the ion diffusion coefficient to be about $D^*_{l,ions} \approx 10^{-10}$ cm^2/s, suggesting a viscous state which slows virus inactivation. While SLF and nasal mucus do not completely suppress the diffusivity of water molecules themselves (see Figure S9D), the very slow diffusion of the Na^+ and Cl^- ions keeps the concentration of the solution high and, thus, also determines the low rate of continued loss of water molecules. It should further be noted that the diffusion coefficients determined in this way are "effective" (indicated by a star) as they represent the molecular diffusivities under the specific morphological conditions associated with the dendritic growth of the salt crystals inside the droplets (see the next section for details on how these diffusion coefficients were further constrained).

Independent of the exact thermodynamic equilibrium state of the particles, our results demonstrate that SLF and nasal mucus show a clear diffusion limitation for ions. In contrast, water diffusion in SLF and nasal mucus remains fast even when RH is low. This continuous, rapid diffusion of water indicates that SLF and nasal mucus do not form diffusion-inhibiting, semisolid-phase states such as those recently reported by others in particles containing model respiratory compounds.[48]

Biophysical Model of Inactivation in Expiratory Aerosol Particles. The combination of the virological bulk-phase data (Figure 1) with the microphysical aerosol thermodynamics (vapor pressures and activity coefficients) and kinetics (Figures 2 and S9) allows the pH attained in the aerosol particles and the resulting rates of viral inactivation to be determined. Thus, the virological and microphysical data were combined as input for a multishell ResAM. ResAM is a biophysical model that simulates the composition and pH changes inside an expiratory particle during exhalation and determines the impact of these changes on virus infectivity (see the section "Biophysical Modeling" and the Supporting Information). The model performs calculations for particles of selectable size (from 20 nm to 1 mm) with a liquid phase composed of organic and inorganic species representative of human respiratory fluids (see Table S1). It takes account of diffusion in the gaseous and condensed phase, vapor pressures, heat transfer, deliquescence, efflorescence, species dissociation, and activity coefficients due to electrolytic ion interactions (see Tables S2 and S3). Ultimately, ResAM computes the species distribution and their activity in the liquid, the resulting pH, and the corresponding virus inactivation rates as a function of time and of the radial coordinate within the particle. A thorough discussion of uncertainties and validity limitations of the combined virus inactivation data from bulk-phase measurements, the aerosol microphysics determined in the EDB, and the multishell biophysical model is provided in the Supporting Information.

When RH changes are slow, the measured mass fraction of solutes in SLF as a function of RH allows the model thermodynamics to be constrained (Figure S4B). Under thermodynamic equilibrium conditions, the model captures the mass fraction of solutes along the deliquesced and effloresced branches of the particle reasonably well. However, only after kinetic effects (ion and water diffusivities) are also taken into account does the model accurately reproduce the solute composition curve along the deliquesced branch. This demonstrates that even when RH changes are slow (raising RH from 50 to 70% in over 1 h), kinetics cannot be neglected.

For rapidly evaporating expiratory particles, kinetic effects are even more critical. By matching the model to the fast changes during the efflorescence and deliquescence processes, ion diffusion coefficients can be derived for different water activities. Interpolation together with literature data under dilute conditions yields D_{l,H_2O}, D_{l,Na^+}, and D_{l,Cl^-} (for details, see Figure S9D). Other neutral species, cations and anions, are

https://doi.org/10.1021/acs.est.2c05777
Environ. Sci. Technol. 2023, 57, 486−497

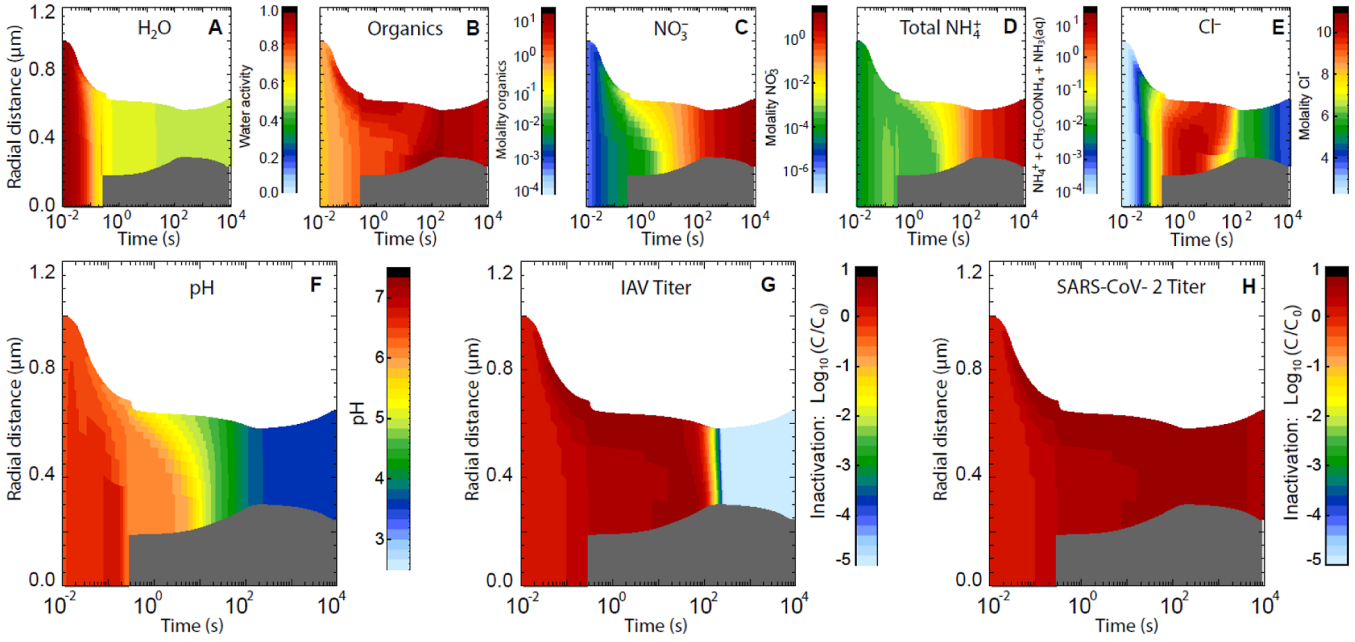

Figure 3. Evolution of physicochemical conditions within a respiratory particle leading to inactivation of trapped viruses during the transition from nasal to typical indoor air conditions, modeled with ResAM. The initial radius of the particle is 1 μm. Thermodynamic and kinetic properties are those of SLF (see Figure 2 and Table S1). The indoor air conditions are set at 20 °C and 50% RH (see Figure S10 for the corresponding depiction of physicochemical conditions at 80% RH). The exhaled air is assumed to mix into the indoor air using a turbulent eddy diffusion coefficient of 50 cm^2/s (see Supporting Information, section "Mixing of the exhaled aerosol with indoor air"). The temporal evolution of gas-phase mixing ratios is shown in Figure S11. The gas-phase compositions of exhaled and typical indoor air are given in Table S4. Within 0.3 s, the particle shrinks to 0.7 μm due to rapid H_2O loss, causing NaCl to effloresce (gray core). The particle then reaches 0.6 μm within 2 min due to further crystal growth, after which it slowly grows again due to coupled HNO_3 and NH_3 uptake and HCl loss. ResAM models the physicochemical changes in particles including (A) water activity, (B) molality of organics, (C) NO_3^- (resulting from the deprotonation of HNO_3), (D) molality of total ammonium, (E) molality of Cl^-, (F) pH, as well as inactivation of (G) IAV and (H) SARS-CoV-2 (decadal logarithm of virus titer C at time t relative to initial virus titer C_0).

treated accordingly, scaled with their infinite dilution values (see the Supporting Information).

As an example, Figure 3 shows the evolution of the physicochemical conditions within an expiratory particle with 1 μm initial radius during transition from nasal to typical indoor air conditions with 50% RH (see trace gases in Table S4) and the concomitant inactivation of IAV and SARS-CoV-2 contained within the particle. The rapid loss of water leads to concentration of the organics and salts to the point when NaCl effloresces. In addition to H_2O, CO_2, which stems from the dissolved bicarbonate, also evaporates from the particle, causing the pH to rise for a short time (<0.3 s) from the initial 6.6 to around 7.0. This is similar to the trend to higher pH observed by Oswin et al.[26] for much larger particles. However, this effect is only intermediate.[49] Nitric acid from the indoor air enters the particle readily, lowering its pH to 5 within ~10 s. This, in turn, pulls NH_3 into the particle, partly compensating the acidification. The pH further decreases to ~4 within 2 min and then slowly approaches pH 3.7 due to further uptake of HNO_3 from the room air. This result confirms the importance of trace gases in determining the pH of indoor aerosol particles.[30] If only CO_2 is considered, its volatilization from the particle would lead to an expected increase in pH after exhalation.[26] Owing to aerosol acidification, rapid influenza virus inactivation occurs at ~2 min, whereas SARS-CoV-2 (and the even more pH-tolerant HCoV-229E) remains infectious.

Inactivation times vary with particle size: larger droplets take longer to reach low pH than smaller ones as they are impeded by longer diffusion paths of the relevant molecules (mainly HNO_3 and NH_3) or ions through both air and liquid phases. The black line in Figure 4D illustrates this relationship for IAV, showing 99% inactivation after about 2 min in particles with radii <1 μm but longer than 5 days for millimeter-sized particles. As a rule of thumb, a 10-fold increase in particle size leads to roughly a 10-fold increase in IAV inactivation time under typical indoor conditions. Conversely, the black line in Figure 4E for SARS-CoV-2 shows that inactivation is inefficient for SARS-CoV-2, irrespective of particle size.

Inactivation times for both IAV and SARS-CoV-2 can be greatly reduced if the indoor air is slightly acidified. This can be achieved by either removing basic gases or adding acidic ones, provided that the gaseous acid molecules meet two conditions: their volatility must be sufficiently low, such that they readily partition from the gas phase to the condensed phase, and once dissolved, they must be sufficiently strong acids to overcome any pH buffering by the particle matrix. Figure 4 compares the aerosol pH in typical indoor air (panel A; NH_3 = 36.3 ppb and HNO_3 = 0.27 ppb) with that in air depleted in NH_3 to 10 ppt (panel B) or enriched to 50 ppb HNO_3 (panel C). This concentration of HNO_3 is well below legal 8 h exposure thresholds (0.5−2 ppm[50,51]).

Scrubbing of NH_3 reduces the time to reach an aerosol pH of 4 from minutes to seconds. Correspondingly, IAV inactivation times decrease by up to an order of magnitude (light blue lines in Figure 4D,E). This acceleration is mostly limited to particles in the 2−5 μm size range, which are minor contributors to the exhaled aerosol (Figure 4F). Furthermore,

https://doi.org/10.1021/acs.est.2c05777
Environ. Sci. Technol. 2023, 57, 486−497

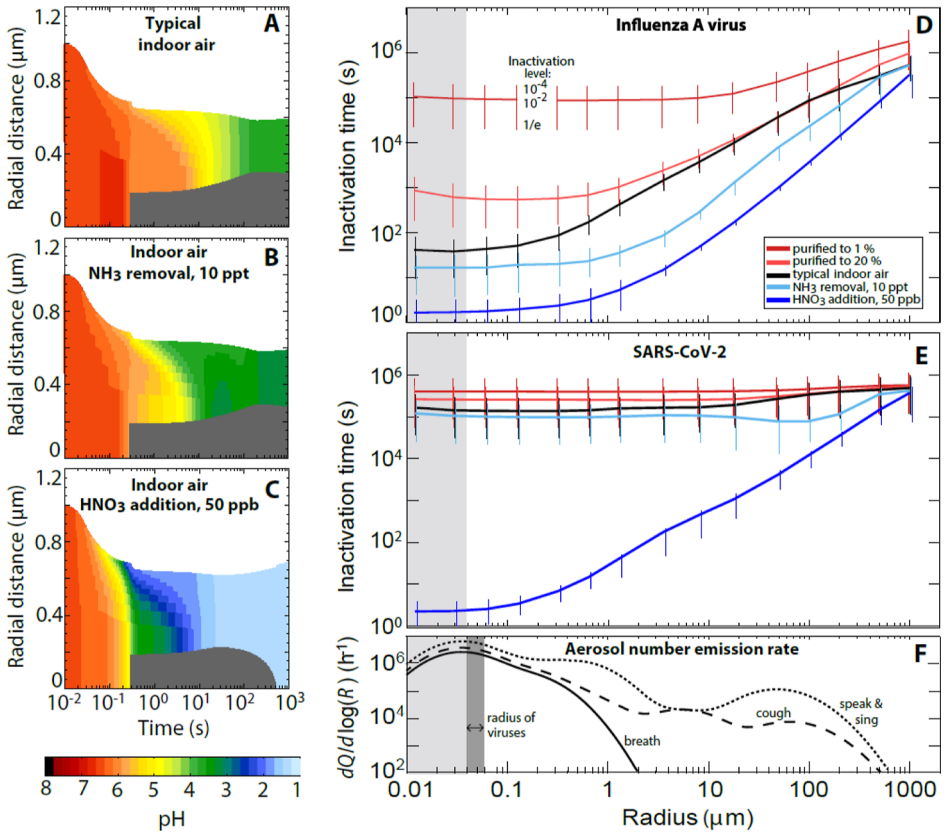

Figure 4. Impact of airborne acidity on virus inactivation in expiratory particles. (A) Modeled pH value in a particle with properties of synthetic lung fluid with initially 1 μm radius exhaled into air (20 °C, 50% RH) with typical indoor composition (same as Figure 3F). (B) Same as (A), but for indoor air with NH_3 reduced to 10 ppt, e.g., by means of an NH_3 scrubber, reducing the time to reach pH 4 from 2 min to less than 10 s. (C) Same as (A), but in indoor air enriched to 50 ppb HNO_3, reducing the time to reach pH 4 from 2 min to less than 0.5 s. (D,E) Inactivation times of IAV and SARS-CoV-2 as a function of particle radius under various conditions: indoor air with typical composition (black), depleted in NH_3 to 10 ppt (light blue), enriched to 50 ppb HNO_3 (dark blue), or purified air with both, HNO_3 and NH_3, reduced to 20 or 1% of typical indoor values (red). Whiskers show reductions of virus load to 10^{-4} (upper end), 10^{-2} (intersection with line), and $1/e$ (lower end). The exhaled air mixes with the indoor air by turbulent eddy diffusion (same as Figure 3); for sensitivity tests on eddy diffusivity, see Figures S14B and S15B. The gas-phase compositions of exhaled air and the various cases of indoor air shown here are defined in Table S4. (F) Mean size distribution of number emission rates of expiratory aerosol particles [$dQ/d\log(R)$] for breathing (solid line), speaking and singing (dotted line), and coughing (dashed line).[57] Dark gray range indicates virus radii. Light gray shading shows conditions for particles smaller than a virus, referring to an equivalent coating volume with inactivation times indicated. [Radius values in (D−F) refer to the particle size 1 s after exhalation].

NH_3 scrubbing does not affect SARS-CoV-2 inactivation because the aerosol pH remains in this virus' stability range (Figure 1).

A much stronger effect is observed for the addition of HNO_3. A HNO_3 concentration of 50 ppb allows the aerosol pH value to drop below 2, which is required for efficient SARS-CoV-2 inactivation (Figure 1). For comparison, enriching air with the more volatile and weaker acetic acid at concentrations below exposure threshold values could not achieve this, see Figure S12. The dark blue lines in Figure 4D,E show the resulting inactivation times for IAV and SARS-CoV-2 (and Figure S13 for HCoV-229E) as a function of particle radius. Remarkably, inactivation times of SARS-CoV-2 diminished by 4−5 orders of magnitude compared to typical indoor air (black lines). For particles with radii <1 μm, which constitutes the majority of expiratory particles (see panel F), inactivation is expected to occur within 30 s.

While enrichment of acidic gases in air leads to an acceleration of IAV and SARS-CoV-2 inactivation, depletion of these gases, for instance by filtering freshly supplied air, has the opposite effect. It is well-known that concentrations of strong inorganic acids, such as HNO_3, are lower indoors than outdoors by at least a factor of 2 and in buildings with special air purification, such as museums and libraries, by factors 10−80.[30] If air is purified to contain only a fraction of the initial trace gas concentrations (see Table S4), the aerosol pH increases compared to typical indoor air and intermittently reaches neutral or even slightly alkaline values (up to pH 8.4 in particles with 5 μm radius in air purified to 1%). As a result, air purification is expected to enhance virus persistence, especially for IAV, as indicated by the red curves in Figure 4D,E.

To validate the model results, we compared published inactivation data for aerosolized IAV and SARS-CoV-2 obtained in rotating drum experiments with inactivation times estimated by ResAM (Figures S16 and S17 and the Supporting Information). Even though rotating drums rely on time-integrated samples and are therefore not ideally suited to measure very rapid inactivation kinetics, modeled and measured inactivation times for both viruses exhibit similar trends as a function of RH. For IAV, measured inactivation times are consistent with ResAM predictions for experiments conducted in partly purified air, as is expected for rotating drum experiments. The comparison with SARS-CoV-2 is inconclusive because of the wide scatter in the experimental

https://doi.org/10.1021/acs.est.2c05777
Environ. Sci. Technol. 2023, 57, 486−497

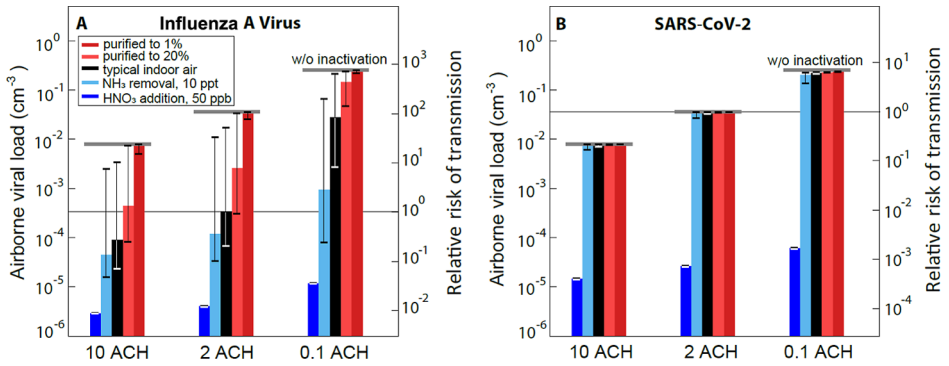

Figure 5. Airborne viral load (# infectious viruses per volume of air) and relative risk of IAV (A) and SARS-CoV-2 (B) transmission under different air treatment scenarios. Calculations are for a room (20 °C, 50% RH) with different ventilation rates (ACH) and subject to various air treatments, assuming the room to accommodate one infected person per 10 m^3 of air, emitting virus-laden aerosol by normal breathing (solid curve in Figure 4E), and assuming one infectious virus per aerosol particle irrespective of size (see Figure S18 for a scenario with a size-dependent virus distribution). Steady-state viral load (left axes) is calculated as the balance of exhaled viruses and their removal by ventilation (0.1−10 ACH), deposition, and inactivation (calculated as for Figure 4D,E, starting from radius 0.05 μm, the radius of viruses). ACH affects the indoor trace gas-phase concentrations [at higher ACH, gases with predominantly outdoor sources (HNO_3 and HCl) have higher concentration and gases with indoor sources (NH_3, CO_2, and CH_3COOH) have lower concentrations]. We assume gas-phase concentrations in Table S4 to refer to 2 ACH and then calculate the gas-phase concentration for 10 ACH and 0.1 ACH by mixing with more or less outdoor air (see the Supporting Information for further details). ACH also determines the mixing speed of the exhalation plume with indoor air (see the Supporting Information). Whiskers show the uncertainty range resulting from the spread of trace gas concentrations in room air (upper limits use the least acidic composition in Table S4, i.e., the highest measured NH_3 and the lowest for all acidic gases and lower limits conversely). Right axes show the transmission risk under these treatments relative to the risk in a room with typical indoor air (see Table S4) and 2 ACH (thin horizontal line). A detailed description of the relative risk calculations is given in the Supporting Information. Typical indoor air is shown by black bars, filtered air with removal of trace gases to 20% or to 1% by red bars, air with NH_3 removed to 10 ppt by light blue bars, and air enriched to 50 ppb HNO_3 by dark blue bars. The whiskers in the case with NH_3 removal include the range of possible HNO_3 release from the background aerosol particles after removing NH_3 from the indoor air (see Table S4). Thick gray horizontal lines indicate the viral load and relative transmission risk in the absence of any inactivation. Results for 2 and 5 ppb HNO_3, see Figure S20, results for HCoV-229E, and analyses for coughing and speaking/singing, see Figure S19.

data. However, ResAM predictions fall within the range of measured inactivation times. Given the importance of semivolatile acids and bases for inactivation, further model validation should include inactivation times measured in aerosol experiments under well-known air compositions, including the presence of HNO_3.

Management of Airborne Transmission Risks. Given the high pH sensitivity of many viruses[23,52−54] and the readiness of expiratory aerosol particles for acidification, we next investigated the extent to which the modification of indoor air composition could mitigate the risk of virus transmission. To this end, we consider a ventilated room with occupants who exhale aerosol containing infectious viruses. We further make the assumption that, given the low concentration of airborne viruses, the transmission risk is directly proportional to the infectious virus concentration, respectively, in inhalation dose. We use the term "relative risk of transmission" to express how the risk changes from standard conditions (here, typical indoor air according to Table S4) compared to air slightly enriched by HNO_3, scrubbed of NH_3, or air that has been purified.

For the ventilated room, we assume steady-state conditions where the exhalation defines the source of virus, which is balanced by three sinks, namely, air exchange through ventilation, aerosol deposition, and pH-moderated virus inactivation within the aerosol particles (see the Supporting Information). We describe the virus source by the mean size distributions of number emission rates of expiratory aerosol particles (Figure 4F) and assume each particle with radius >50 nm to carry one virus irrespective of size (see Figure S18 for a sensitivity test relaxing this assumption). We describe the virus sinks by expressing ventilation by air change per hour (ACH, mixing ventilation), applying mean aerosol deposition rates,[55] and computing the inactivation rates as for Figure 4D,E. This allows the airborne viral load and, thus, the relative risk of transmission to be calculated, as displayed in Figure 5 for IAV and SARS-CoV-2 (and Figure S19 for HCoV-229E). Black bars show the results for typical indoor conditions, light blue bars indicate air from which NH_3 was scrubbed to 10 ppt, dark blue bars an enrichment of HNO_3 to 50 ppb, and red bars indicate purification of air to 20 or 1% of trace gases (see Table S4).

Figure 5 highlights the importance of ventilation, which does not only lead to a dilution of the viral load but in addition has the important role of resupplying acidic gases from outside. A further improvement is reached by enriching HNO_3 to 50 ppb, which diminishes the relative risk of transmission of IAV by a factor of ∼80 and of SARS-CoV-2 by a factor of ∼1000 in rooms with 2 ACH. Interestingly, HNO_3 addition outperforms an increase in ventilation from 2 ACH to 10 ACH. Notably, inactivation times of IAV and SARS-CoV-2 drop to only a few seconds for small particles (Figure 4D,E) and are now on the same time scale as HNO_3 transport through the gas phase to the droplet by ACH-induced eddy diffusion (see the Supporting Information). In this scenario, higher ACH leads to a faster mixing of the HNO_3-enriched air into the exhaled plume, resulting in faster acidification of the exhaled aerosol, and hence a lower relative risk of transmission at higher ACH (dark blue bars in Figure 5). In contrast, enrichment to 50 ppb HNO_3 only has a moderate impact on HCoV-229E (Figures S13 and S19).

In comparison, NH_3 scrubbing reduces the relative risk of IAV transmission by a factor of 2−3, depending on the human activity (Figures S19 and S18). This approach, however, is

https://doi.org/10.1021/acs.est.2c05777
Environ. Sci. Technol. 2023, 57, 486−497

ineffective for SARS-CoV-2 or HCoV-229E, highlighting the importance of ventilation in such a scenario.

Finally, the ResAM estimates for purified air with significant reduction of trace gases (red bars) are also striking. While even normal air conditioning systems with air filters can lead to a reduction in "sticky" molecules such as HNO_3,[56] acid removal is likely even more pronounced in museums, libraries, or hospitals with activated carbon filters.[30] In such public buildings, the relative risk of IAV transmission can increase significantly compared to buildings supplied with unfiltered outdoor air.

In summary, we demonstrate that the control of aerosol pH is a critical tool in the mitigation of airborne virus transmission. We predict that a significant abatement in transmission risk can be achieved by air acidification and we are currently working to validate this prediction in aerosol experiments. For strongly pH-sensitive viruses (e.g., IAV), mere scrubbing of NH_3 from indoor air suffices to bring about a modest reduction in the airborne viral load. A greater effect that also extends to more acid-tolerant viruses (e.g., SARS-CoV-2) results from air enrichment with an acidic gas. Here, we evaluated the use of HNO_3 for this purpose because it is already ubiquitous in the outdoor environment, even though alternative acids may achieve similar results and may enjoy higher user acceptability. An effective reduction in viral load can already be achieved by applying HNO_3 at levels lower than 10% of the legal exposure thresholds.[50,51] We therefore expect that the resulting acid exposure will not cause harmful effects on human health. Nevertheless, future studies should investigate the consequences of acid accumulation in indoor air on the microbiome and immune response in the respiratory tract. Additionally, methods are needed for real-time monitoring of aerosol pH, both to prevent acid overexposure and to ensure efficient virus inactivation. Also, finally, successful virus control through air acidification will also require educating the public about the value of adopting appropriate measures for indoor air quality. Nevertheless, even if acidification is never adopted owing to these concerns, the arguments toward ammonia stripping—which in itself may be sufficient to inactivate influenza virus rapidly—is an indirect way to increase acidity and allow acidic gases occurring in the environment to maximize their impact.

Despite the current unknowns, targeted regulation of aerosol pH promises profound positive effects on airborne virus control. Practices that help acidify exhaled aerosols should thus be considered as a strategy to mitigate virus transmission and disease—alongside interventions such as ventilation that mechanically reduce the concentration of airborne viruses (i.e., dilution) and ensure the resupply of acid molecules from outdoor air.

■ ASSOCIATED CONTENT

Supporting Information

The Supporting Information is available free of charge at https://pubs.acs.org/doi/10.1021/acs.est.2c05777.

Method descriptions for virus and matrix preparation, measurement of viral aggregates and electron microscopy for SLF characterization; further details for EDB measurements; in-depth description of ResAM, its uncertainties, and limitations; descriptive comparison of ResAM results with published data; investigation of acetic acid as a potential agent against airborne viruses; particle-shell model; extent and effect of virus aggregation at low pH and high ionic strength; exemplary inactivation curves; additional EDB measurements; (electron) microscopy images of SLF; evolution of physicochemical conditions within aerosols at 80% RH; modeled inactivation times in the presence of acetic acid; modeled inactivation times of HCoV-229E; ResAM sensitivity study results; visual comparison of literature inactivation data and ResAM results; viral load and transmission risk for breathing, coughing, and singing at different air compositions and ventilation rates; substantiation of the assumptions of the ResAM model; composition of SLF; equilibrium constants; liquid-phase diffusion coefficients; and air compositions used in the ResAM model (PDF)

■ AUTHOR INFORMATION

Corresponding Authors

Thomas Peter − *Institute for Atmospheric and Climate Science, ETH Zurich, CH-8092 Zurich, Switzerland*; Email: thomas.peter@env.ethz.ch

Tamar Kohn − *Environmental Chemistry Laboratory, School of Architecture, Civil and Environmental Engineering, Ecole Polytechnique Fédérale de Lausanne (EPFL), CH-1015 Lausanne, Switzerland*; orcid.org/0000-0003-0395-6561; Email: tamar.kohn@epfl.ch

Authors

Beiping Luo − *Institute for Atmospheric and Climate Science, ETH Zurich, CH-8092 Zurich, Switzerland*

Aline Schaub − *Environmental Chemistry Laboratory, School of Architecture, Civil and Environmental Engineering, Ecole Polytechnique Fédérale de Lausanne (EPFL), CH-1015 Lausanne, Switzerland*; orcid.org/0000-0002-1468-6678

Irina Glas − *Institute of Medical Virology, University of Zurich, CH-8057 Zurich, Switzerland*; orcid.org/0000-0001-6976-6360

Liviana K. Klein − *Institute for Atmospheric and Climate Science, ETH Zurich, CH-8092 Zurich, Switzerland*; orcid.org/0000-0002-7205-1718

Shannon C. David − *Environmental Chemistry Laboratory, School of Architecture, Civil and Environmental Engineering, Ecole Polytechnique Fédérale de Lausanne (EPFL), CH-1015 Lausanne, Switzerland*; orcid.org/0000-0003-3345-9443

Nir Bluvshtein − *Institute for Atmospheric and Climate Science, ETH Zurich, CH-8092 Zurich, Switzerland*; orcid.org/0000-0002-7999-4460

Kalliopi Violaki − *Laboratory of Atmospheric Processes and Their Impacts, School of Architecture, Civil and Environmental Engineering, Ecole Polytechnique Fédérale de Lausanne (EPFL), CH-1015 Lausanne, Switzerland*

Ghislain Motos − *Laboratory of Atmospheric Processes and Their Impacts, School of Architecture, Civil and Environmental Engineering, Ecole Polytechnique Fédérale de Lausanne (EPFL), CH-1015 Lausanne, Switzerland*

Marie O. Pohl − *Institute of Medical Virology, University of Zurich, CH-8057 Zurich, Switzerland*

Walter Hugentobler − *Laboratory of Atmospheric Processes and Their Impacts, School of Architecture, Civil and Environmental Engineering, Ecole Polytechnique Fédérale de Lausanne (EPFL), CH-1015 Lausanne, Switzerland*; orcid.org/0000-0002-7379-752X

Athanasios Nenes − *Laboratory of Atmospheric Processes and Their Impacts, School of Architecture, Civil and*

https://doi.org/10.1021/acs.est.2c05777
Environ. Sci. Technol. 2023, 57, 486−497

Environmental Engineering, Ecole Polytechnique Fédérale de Lausanne (EPFL), CH-1015 Lausanne, Switzerland; Institute of Chemical Engineering Sciences, Foundation for Research and Technology Hellas, GR-26504 Patras, Greece; orcid.org/0000-0003-3873-9970

Ulrich K. Krieger − *Institute for Atmospheric and Climate Science, ETH Zurich, CH-8092 Zurich, Switzerland;* orcid.org/0000-0003-4958-2657

Silke Stertz − *Institute of Medical Virology, University of Zurich, CH-8057 Zurich, Switzerland;* orcid.org/0000-0001-9491-2892

Complete contact information is available at: https://pubs.acs.org/10.1021/acs.est.2c05777

Author Contributions

B.L., A.S., I.G., and L.K.K. contributed equally to this work. Conceptualization: A.N., S.S., T.K., T.P., U.K.K., and W.H. Methodology: A.S., B.L., I.G., L.K.K., M.O.P., N.B., S.C.D., S.S., T.K., T.P., and U.K.K. Investigation: A.S., B.L., I.G., K.V., L.K.K., M.O.P., N.B., and S.C.D. Visualization: A.S., B.L., I.G., G.M., L.K.K., K.V., S.C.D., T.K., and T.P. Funding acquisition: A.N., S.S., T.K., T.P., U.K.K., and W.H. Project administration: T.K. Supervision: A.N., S.S., T.K., T.P., and U.K.K. Writing—original draft: B.L., S.S., T.K., and T.P. Writing—review and editing: A.N., A.S., GM, I.G., L.K.K., M.O.P., N.B., S.C.D., S.S., T.P., T.K., U.K.K., and W.H.

Notes

The authors declare no competing financial interest.

Data availability: Experimental data are available at https://doi.org/10.5281/zenodo.7382905. ResAM code is available at https://doi.org/10.5281/zenodo.7406941.

■ ACKNOWLEDGMENTS

This work was funded by the Swiss National Science Foundation (grant numbers 189939 and 196729). The authors thank Chuck Haas and Mutian Niu for valuable discussions and acknowledge Ramona Klein for the illustration of virus transmission.

■ REFERENCES

(1) Paget, J.; Spreeuwenberg, P.; Charu, V.; Taylor, R. J.; Iuliano, A. D.; Bresee, J.; Simonsen, L.; Viboud, C. Global mortality associated with seasonal influenza epidemics: New burden estimates and predictors from the GLaMOR Project. *J. Global Health* **2019**, *9*, 020421.

(2) Clarification of terminology: in physical chemistry, an "aerosol" is a system of colloidal particles dispersed in a fluid, such as air. An "aerosol particle" refers to one single condensed-phase element in such an ensemble, which may be solid, liquid, or mixed phase. Correspondingly, a "droplet" refers to any liquid aerosol particle, regardless of particle size. In contrast, in epidemiological or virological parlance, "aerosol" or "aerosol particle" usually means a very small (d less than 1 μm) airborne particle, whereas "droplet" is used as its larger counterpart (d greater than 1 μm). To avoid this confusion, we use the term "particle" to refer to any liquid- or mixed-phase respiratory particle of whatever size. Furthermore, we avoid the virological term "virus particle" and use "virus" instead.

(3) Wang, C. C.; Prather, K. A.; Sznitman, J.; Jimenez, J. L.; Lakdawala, S. S.; Tufekci, Z.; Marr, L. C. Airborne Transmission of Respiratory Viruses. *Science* **2021**, *373*, No. eabd9149.

(4) Smither, S. J.; Eastaugh, L. S.; Findlay, J. S.; Lever, M. S. Experimental Aerosol Survival of SARS-CoV-2 in Artificial Saliva and Tissue Culture Media at Medium and High Humidity. *Emerging Microbes Infect.* **2020**, *9*, 1415−1417.

(5) Kormuth, K. A.; Lin, K.; Prussin, A. J.; Vejerano, E. P.; Tiwari, A. J.; Cox, S. S.; Myerburg, M. M.; Lakdawala, S. S.; Marr, L. C. Influenza Virus Infectivity Is Retained in Aerosols and Droplets Independent of Relative Humidity. *J. Infect. Dis.* **2018**, *218*, 739−747.

(6) Brown, J. R.; Tang, J. W.; Pankhurst, L.; Klein, N.; Gant, V.; Lai, K. M.; McCauley, J.; Breuer, J. Influenza Virus Survival in Aerosols and Estimates of Viable Virus Loss Resulting from Aerosolization and Air-Sampling. *J. Hosp. Infect.* **2015**, *91*, 278−281.

(7) Shechmeister, I. L. Studies on the Experimental Epidemiology of Respiratory Infections: III. Certain Aspects of the Behavior of Type A Influenza Virus as an Air-Borne Cloud. *J. Infect. Dis.* **1950**, *87*, 128−132.

(8) Hemmes, J. H.; Winkler, K. C.; Kool, S. M. Virus Survival as a Seasonal Factor in Influenza and Poliomyelitis. *Nature* **1960**, *188*, 430−431.

(9) Harper, G. J. Airborne Micro-Organisms: Survival Tests with Four Viruses. *J. Hyg.* **1961**, *59*, 479−486.

(10) Schaffer, F. L.; Soergel, M. E.; Straube, D. C. Survival of Airborne Influenza Virus: Effects of Propagating Host, Relative Humidity, and Composition of Spray Fluids. *Arch. Virol.* **1976**, *51*, 263−273.

(11) Schuit, M.; Gardner, S.; Wood, S.; Bower, K.; Williams, G.; Freeburger, D.; Dabisch, P. The Influence of Simulated Sunlight on the Inactivation of Influenza Virus in Aerosols. *J. Infect. Dis.* **2020**, *221*, 372−378.

(12) Schuit, M.; Ratnesar-Shumate, S.; Yolitz, J.; Williams, G.; Weaver, W.; Green, B.; Miller, D.; Krause, M.; Beck, K.; Wood, S.; Holland, B.; Bohannon, J.; Freeburger, D.; Hooper, I.; Biryukov, J.; Altamura, L. A.; Wahl, V.; Hevey, M.; Dabisch, P. Airborne SARS-CoV-2 Is Rapidly Inactivated by Simulated Sunlight. *J. Infect. Dis.* **2020**, *222*, 564−571.

(13) Dabisch, P.; Schuit, M.; Herzog, A.; Beck, K.; Wood, S.; Krause, M.; Miller, D.; Weaver, W.; Freeburger, D.; Hooper, I.; Green, B.; Williams, G.; Holland, B.; Bohannon, J.; Wahl, V.; Yolitz, J.; Hevey, M.; Ratnesar-Shumate, S. The Influence of Temperature, Humidity, and Simulated Sunlight on the Infectivity of SARS-CoV-2 in Aerosols. *Aerosol Sci. Technol.* **2020**, *55*, 142.

(14) van Doremalen, N.; Bushmaker, T.; Morris, D. H.; Holbrook, M. G.; Gamble, A.; Williamson, B. N.; Tamin, A.; Harcourt, J. L.; Thornburg, N. J.; Gerber, S. I.; Lloyd-Smith, J. O.; de Wit, E.; Munster, V. J. Aerosol and Surface Stability of SARS-CoV-2 as Compared with SARS-CoV-1. *N. Engl. J. Med.* **2020**, *382*, 1564−1567.

(15) Ijaz, M. K.; Brunner, A. H.; Sattar, S. A.; Nair, R. C.; Johnson-Lussenburg, C. M. Survival Characteristics of Airborne Human Coronavirus 229E. *J. Gen. Virol.* **1985**, *66*, 2743−2748.

(16) Marr, L. C.; Tang, J. W.; Van Mullekom, J.; Lakdawala, S. S. Mechanistic Insights into the Effect of Humidity on Airborne Influenza Virus Survival, Transmission and Incidence. *J. R. Soc., Interface* **2019**, *16*, 20180298.

(17) Lin, K.; Marr, L. C. Humidity-Dependent Decay of Viruses, but Not Bacteria, in Aerosols and Droplets Follows Disinfection Kinetics. *Environ. Sci. Technol.* **2020**, *54*, 1024−1032.

(18) Morris, D. H.; Yinda, K. C.; Gamble, A.; Rossine, F. W.; Huang, Q.; Bushmaker, T.; Fischer, R. J.; Matson, M. J.; Van Doremalen, N.; Vikesland, P. J.; Marr, L. C.; Munster, V. J.; Lloyd-Smith, J. O. Mechanistic Theory Predicts the Effects of Temperature and Humidity on Inactivation of SARS-CoV-2 and Other Enveloped Viruses. *eLife* **2021**, *10*, No. e65902.

(19) Niazi, S.; Groth, R.; Cravigan, L.; He, C.; Tang, J. W.; Spann, K.; Johnson, G. R. Susceptibility of an Airborne Common Cold Virus to Relative Humidity. *Environ. Sci. Technol.* **2021**, *55*, 499−508.

(20) Niazi, S.; Short, K. R.; Groth, R.; Cravigan, L.; Spann, K.; Ristovski, Z.; Johnson, G. R. Humidity-Dependent Survival of an Airborne Influenza A Virus: Practical Implications for Controlling Airborne Viruses. *Environ. Sci. Technol. Lett.* **2021**, *8*, 412−418.

(21) Yang, W.; Elankumaran, S.; Marr, L. C. Relationship between Humidity and Influenza A Viability in Droplets and Implications for Influenza's Seasonality. *PloS One* **2012**, *7*, No. e46789.

(22) Weber, R. J.; Guo, H.; Russell, A. G.; Nenes, A. High Aerosol Acidity despite Declining Atmospheric Sulfate Concentrations over the Past 15 Years. *Nat. Geosci.* **2016**, *9*, 282−285.
(23) Scholtissek, C. Stability of Infectious Influenza A Viruses to Treatment at Low PH and Heating. *Arch. Virol.* **1985**, *85*, 1−11.
(24) Yang, W.; Marr, L. C. Mechanisms by Which Ambient Humidity May Affect Viruses in Aerosols. *Appl. Environ. Microbiol.* **2012**, *78*, 6781−6788.
(25) Pye, H. O. T.; Nenes, A.; Alexander, B.; Ault, A. P.; Barth, M. C.; Clegg, S. L.; Collett, J. L., Jr.; Fahey, K. M.; Hennigan, C. J.; Herrmann, H.; Kanakidou, M.; Kelly, J. T.; Ku, I.-T.; McNeill, V. F.; Riemer, N.; Schaefer, T.; Shi, G.; Tilgner, A.; Walker, J. T.; Wang, T.; Weber, R.; Xing, J.; Zaveri, R. A.; Zuend, A. The Acidity of Atmospheric Particles and Clouds. *Atmos. Chem. Phys.* **2020**, *20*, 4809−4888.
(26) Oswin, H. P.; Haddrell, A. E.; Otero-Fernandez, M.; Mann, J. F. S.; Cogan, T. A.; Hilditch, T. G.; Tian, J.; Hardy, D. A.; Hill, D. J.; Finn, A.; Davidson, A. D.; Reid, J. P. The Dynamics of SARS-CoV-2 Infectivity with Changes in Aerosol Microenvironment. *Proc. Natl. Acad. Sci. U.S.A.* **2022**, *119*, No. e2200109119.
(27) Huang, Y.The SARS Epidemic and Its Aftermath in China: A Political Perspective. In *Learning from SARS—Preparing for the Next Disease Outbreak: Workshop Summary*; Institute of Medicine, The National Academies Press: Washington DC, 2004; pp 116−136.
(28) Nah, T.; Guo, H.; Sullivan, A. P.; Chen, Y.; Tanner, D. J.; Nenes, A.; Russell, A.; Ng, N.; Huey, L.; Weber, R. J. Characterization of Aerosol Composition, Aerosol Acidity, and Organic Acid Partitioning at an Agriculturally Intensive Rural Southeastern US Site. *Atmos. Chem. Phys.* **2018**, *18*, 11471−11491.
(29) Brauer, M.; Koutrakis, P.; Keeler, G. J.; Spengler, J. D. Indoor and Outdoor Concentrations of Inorganic Acidic Aerosols and Gases. *J. Air Waste Manage. Assoc.* **1991**, *41*, 171−181.
(30) Nazaroff, W. W.; Weschler, C. J. Indoor Acids and Bases. *Indoor Air* **2020**, *30*, 559−644.
(31) Ampollini, L.; Katz, E. F.; Bourne, S.; Tian, Y.; Novoselac, A.; Goldstein, A. H.; Lucic, G.; Waring, M. S.; DeCarlo, P. F. Observations and Contributions of Real-Time Indoor Ammonia Concentrations during HOMEChem. *Environ. Sci. Technol.* **2019**, *53*, 8591−8598.
(32) Vaughan, J.; Ngamtrakulpanit, L.; Pajewski, T. N.; Turner, R.; Nguyen, T. A.; Smith, A.; Urban, P.; Hom, S.; Gaston, B.; Hunt, J. Exhaled Breath Condensate PH Is a Robust and Reproducible Assay of Airway Acidity. *Eur. Respir. J.* **2003**, *22*, 889−894.
(33) Colberg, C. A.; Krieger, U. K.; Peter, T. Morphological Investigations of Single Levitated H2SO4/NH3/H2O Aerosol Particles during Deliquescence/Efflorescence Experiments. *J. Phys. Chem. A* **2004**, *108*, 2700−2709.
(34) Steimer, S. S.; Krieger, U. K.; Te, Y. F.; Lienhard, D. M.; Huisman, A. J.; Luo, B. P.; Ammann, M.; Peter, T. Electrodynamic Balance Measurements of Thermodynamic, Kinetic, and Optical Aerosol Properties Inaccessible to Bulk Methods. *Atmos. Meas. Tech.* **2015**, *8*, 2397−2408.
(35) Davis, E. J.; Buehler, M. F.; Ward, T. L. The double-ring electrodynamic balance for microparticle characterization. *Rev. Sci. Instrum.* **1990**, *61*, 1281−1288.
(36) Zobrist, B.; Soonsin, V.; Luo, B. P.; Krieger, U. K.; Marcolli, C.; Peter, T.; Koop, T. Ultra-Slow Water Diffusion in Aqueous Sucrose Glasses. *Phys. Chem. Chem. Phys.* **2011**, *13*, 3514.
(37) Tang, I. N.; Munkelwitz, H. R. Water Activities, Densities, and Refractive Indices of Aqueous Sulfates and Sodium Nitrate Droplets of Atmospheric Importance. *J. Geophys. Res.: Atmos.* **1994**, *99*, 18801−18808.
(38) Zardini, A. A.; Sjogren, S.; Marcolli, C.; Krieger, U. K.; Gysel, M.; Weingartner, E.; Baltensperger, U.; Peter, T. A Combined Particle Trap/HTDMA Hygroscopicity Study of Mixed Inorganic/Organic Aerosol Particles. *Atmos. Chem. Phys.* **2008**, *8*, 5589−5601.
(39) Chýlek, P. Partial-Wave Resonances and the Ripple Structure in the Mie Normalized Extinction Cross Section. *J. Opt. Soc. Am.* **1976**, *66*, 285−287.
(40) Bastelberger, S.; Krieger, U. K.; Luo, B.; Peter, T. Diffusivity Measurements of Volatile Organics in Levitated Viscous Aerosol Particles. *Atmos. Chem. Phys.* **2017**, *17*, 8453−8471.
(41) Dou, J.; Alpert, P. A.; Corral Arroyo, P.; Luo, B.; Schneider, F.; Xto, J.; Huthwelker, T.; Borca, C. N.; Henzler, K. D.; Raabe, J.; Watts, B.; Herrmann, H.; Peter, T.; Ammann, M.; Krieger, U. K. Photochemical Degradation of Iron(III) Citrate/Citric Acid Aerosol Quantified with the Combination of Three Complementary Experimental Techniques and a Kinetic Process Model. *Atmos. Chem. Phys.* **2021**, *21*, 315−338.
(42) Carslaw, K. S.; Clegg, S. L.; Brimblecombe, P. A Thermodynamic Model of the System HCl-HNO3-H2SO4-H2O, Including Solubilities of HBr, from <200 to 328 K. *J. Phys. Chem.* **1995**, *99*, 11557−11574.
(43) Luo, B.; Carslaw, K. S.; Peter, T.; Clegg, S. L. Vapour Pressures of H2SO4/HNO3/HCl/HBr/H2O Solutions to Low Stratospheric Temperatures. *Geophys. Res. Lett.* **1995**, *22*, 247−250.
(44) Lin, K.; Schulte, C. R.; Marr, L. C. Survival of MS2 and Φ6 viruses in droplets as a function of relative humidity, pH, and salt, protein, and surfactant concentrations. *PLoS One* **2020**, *15*, No. e0243505.
(45) Galloway, S. E.; Reed, M. L.; Russell, C. J.; Steinhauer, D. A. Influenza HA Subtypes Demonstrate Divergent Phenotypes for Cleavage Activation and PH of Fusion: Implications for Host Range and Adaptation. *PLoS Pathog.* **2013**, *9*, No. e1003151.
(46) Bullough, P. A.; Hughson, F. M.; Skehel, J. J.; Wiley, D. C. Structure of Influenza Haemagglutinin at the PH of Membrane Fusion. *Nature* **1994**, *371*, 37−43.
(47) Jackson, C. B.; Farzan, M.; Chen, B.; Choe, H. Mechanisms of SARS-CoV-2 Entry into Cells. *Nat. Rev. Mol. Cell Biol.* **2022**, *23*, 3−20.
(48) Huynh, E.; Olinger, A.; Woolley, D.; Kohli, R. K.; Choczynski, J. M.; Davies, J. F.; Lin, K.; Marr, L. C.; Davis, R. D. Evidence for a Semisolid Phase State of Aerosols and Droplets Relevant to the Airborne and Surface Survival of Pathogens. *Proc. Natl. Acad. Sci. U.S.A.* **2022**, *119*, No. e2109750119.
(49) Klein, L. K.; Luo, B.; Bluvshtein, N.; Krieger, U. K.; Schaub, A.; Glas, I.; David, S. C.; Violaki, K.; Motos, G.; Pohl, M. O.; Hugentobler, W.; Nenes, A.; Stertz, S.; Peter, T.; Kohn, T. Expiratory Aerosol PH Is Determined by Indoor Room Trace Gases and Particle Size. *Proc. Natl. Acad. Sci. U.S.A.* **2022**, *119*, No. e2212140119.
(50) The National Institute for Occupational Safety and Health (NIOSH). CDC—NIOSH Pocket Guide to Chemical Hazards—Nitric acid. Time-Weighted Average (TWA) of the Permissible Exposure Limit (PEL), Legal 8-hour Limit in the United States for Exposure of an Employee 2 ppm for HNO_3. https://www.cdc.gov/niosh/npg/npgd0447.html (accessed Nov 2, 2022).
(51) German Social Accident Insurance (DGUV). GESTIS International Limit Values. National Occupational Exposure Limits (OELs) in the European Union, Legal 8 h Limit, 0.5−2 ppm for HNO_3, Depending on Country. https://limitvalue.ifa.dguv.de/WebForm_ueliste2.aspx (accessed Nov 2, 2022).
(52) Nicola, A. V.; McEvoy, A. M.; Straus, S. E. Roles for Endocytosis and Low PH in Herpes Simplex Virus Entry into HeLa and Chinese Hamster Ovary Cells. *J. Virol.* **2003**, *77*, 5324−5332.
(53) Ausar, S. F.; Rexroad, J.; Frolov, V. G.; Look, J. L.; Konar, N.; Middaugh, C. R. Analysis of the Thermal and PH Stability of Human Respiratory Syncytial Virus. *Mol. Pharm.* **2005**, *2*, 491−499.
(54) Darnell, M. E. R.; Subbarao, K.; Feinstone, S. M.; Taylor, D. R. Inactivation of the Coronavirus That Induces Severe Acute Respiratory Syndrome, SARS-CoV. *J. Virol. Methods* **2004**, *121*, 85−91.
(55) Seinfeld, J. H.; Pandis, S. N.*Atmospheric Chemistry and Physics: From Air Pollution to Climate Change*, 6th ed.; Wiley: Hoboken, NJ, 2006.
(56) Neuman, J. A.; Huey, L. G.; Ryerson, T. B.; Fahey, D. W. Study of Inlet Materials for Sampling Atmospheric Nitric Acid. *Environ. Sci. Technol.* **1999**, *33*, 1133−1136.

(57) Pöhlker, M. L.; Krüger, O. O.; Förster, J.-D.; Berkemeier, T.; Elbert, W.; Fröhlich-Nowoisky, J.; Pöschl, U.; Pöhlker, C.; Bagheri, G.; Bodenschatz, E.; Huffman, J. A.; Scheithauer, S.; Mikhailov, E.Respiratory Aerosols and Droplets in the Transmission of Infectious Diseases, 2021. arXiv:210301188. arXiv Prepr. https://doi.org/10.48550/arXiv.2103.01188.

https://doi.org/10.1021/acs.est.2c05777
Environ. Sci. Technol. 2023, 57, 486−497